# Soft, skin-interfaced microfluidic systems with integrated immunoassays, fluorometric sensors and impedance measurement capabilities

Sungbong Kim, Boram Lee, Jonathan T Reeder, Seon Hee Seo, Sung-Uk Lee, Aurélie Hourlier-Fargette, Joonchul Shin, Yurina Sekine, Hyoyoung Jeong, Yong Suk Oh, et al.

▶ **To cite this version:**

Sungbong Kim, Boram Lee, Jonathan T Reeder, Seon Hee Seo, Sung-Uk Lee, et al.. Soft, skin-interfaced microfluidic systems with integrated immunoassays, fluorometric sensors and impedance measurement capabilities. Proceedings of the National Academy of Sciences of the United States of America, 2020, 117 (45), pp.27906-27915. 10.1073/pnas.2012700117 . hal-03414153

**HAL Id: hal-03414153**
**https://hal.science/hal-03414153v1**

Submitted on 4 Nov 2021

**HAL** is a multi-disciplinary open access archive for the deposit and dissemination of scientific research documents, whether they are published or not. The documents may come from teaching and research institutions in France or abroad, or from public or private research centers.

L'archive ouverte pluridisciplinaire **HAL**, est destinée au dépôt et à la diffusion de documents scientifiques de niveau recherche, publiés ou non, émanant des établissements d'enseignement et de recherche français ou étrangers, des laboratoires publics ou privés.

# Soft, skin-interfaced microfluidic systems with integrated immunoassays, fluorometric sensors and impedance measurement capabilities

Sungbong Kim[a,b,1], Boram Lee[c,1], Jonathan T. Reeder[a,d,1], Seon Hee Seo[e,1], Sung-Uk Lee[f], Aurélie Hourlier-Fargette[a,d,g], Joonchul Shin[h], Yurina Sekine[i], Hyoyoung Jeong[a,d], Yong Suk Oh[a,j], Alexander J. Aranyosi[a,k], Stephen P. Lee[a,k], Jeffrey B. Model[a,k], Geumbee Lee[a,d], Min-Ho Seo[a,d], Sung Soo Kwak[a,d], Seongbin Jo[l], Gyungmin Park[l], Sunghyun Han[l], Inkyu Park[j], Hyo-Il Jung[m], Roozbeh Ghaffari[a,k,n,*], Jahyun Koo[o,*], Paul V. Braun[b,*], John A. Rogers[a,k,p,*]

[a] Querrey Simpson Institute for Bioelectronics, Northwestern University, Evanston, IL 60208, USA.
[b] Department of Materials Science and Engineering and Materials Research Laboratory, University of Illinois at Urbana-Champaign, Urbana, IL 61801, USA.
[c] Department of Medicine, Konkuk University, Seoul 05029, Republic of Korea.
[d] Department of Materials Science and Engineering, Northwestern University, Evanston, IL 60208, USA.
[e] Nano Hybrid Technology Research Center, Electrical Materials Research Division, Korea Electrotechnology Research Institute, Changwon 51543, Republic of Korea.
[f] ATF Technology Development Division, Korea Atomic Energy Research Institute, Daejeon, 34057, Republic of Korea.
[g] Université de Strasbourg, CNRS, Institut Charles Sadron UPR22, F-67000 Strasbourg, France.
[h] Center for Electronic Materials, Korea Institute of Science and Technology, Seoul 02792, Republic of Korea.
[i] Materials Sciences Research Center, Japan Atomic Energy Agency, Tokai, Ibaraki 319-1195, Japan.
[j] Department of Mechanical Engineering, Korea Advanced Institute of Science and Technology, Daejeon, 34141, Republic of Korea.
[k] Epicore Biosystems, Inc. Cambridge, MA 02139, USA.
[l] Department of Chemical and Biomolecular Engineering and Materials Research Laboratory, University of Illinois at Urbana-Champaign, Urbana, IL 61801, USA.
[m] School of Mechanical Engineering, Yonsei University, Seoul 03722, Republic of Korea.
[n] Department of Biomedical Engineering, Northwestern University, Evanston, IL 60208, USA.
[o] School of Biomedical Engineering, Korea University, Seoul 02841, Republic of Korea.
[p] Department of Materials Science and Engineering, Department of Biomedical Engineering, Department of Neurological Surgery, Department of Chemistry, Department of Mechanical Engineering, Department of Electrical Engineering and Computer Science, Querrey Simpson Institute and Feinberg Medical School, Northwestern University, Evanston, IL 60208, USA.
[1] S.K., B.L., J.T.R, and S.H.S. contributed equally to this work.
* To whom correspondence may be addressed. **E-mail**: jrogers@northwestern.edu, pbraun@illinois.edu, jahyunkoo@korea.ac.kr, rooz@northwestern.edu

**ORCID**
0000-0003-3082-349X (S.K.)
0000-0002-0148-4145 (A.H.-F.)
0000-0001-5380-2363 (R.G.)

**Classification**
Engineering

**Keywords**
Healthcare, Soft materials, Epidermal devices, Sweat cortisol, Galvanic skin response

**Author Contributions**

S.K., B.L., J.T.R., S.H.S., R.G., J.K., P.V.B. and J.A.R. led development of concepts, organization of system, designed experiments and interpreted results. B.L. (MD PhD) designed human tests, and provided medical consultations, advice and discussion. S.K., B.L., S.H.S., J.K. led over all experiments, fabrications, integrating of subsystems, and finishing with support from J.T.R., A.H.-F., H.J., G.L., Y.S.O., A.J.A, S.P.L., J.B.M., M.-H.S., S.S.K., S.J., G.P. and S.H. Also, S.-U.L., Y.S.O., I.P. performed 3D mechanical modeling and analysis, Y.S.O. provided original idea of skeletal microfluidics and J.S., Y.S., H,-I,J. provided immunoassay and fluorescence assay information and discussion. S.K., B.L., J.T.R., S.H.S., S.-U.L., A.H.-F., Y.S., Y.O., A.J.A, S.P.L., J.B.M., S.J., R.G., J.K. P.V.B and J.A.R led paper writing.

**Competing interests**

J.A.R., J.T.R., Y.S. and S.K. are inventors on a Patent Cooperation Treaty (PCT) patent by the board of trustees of Northwestern University (PCT/US2018/035661), and J.A.R., J.T.R., S.K., Y.S. and A.H-F. are inventors on a PCT patent by the board of trustees of Northwestern University (PCT/US2018/035738). R.G., A.J.A, J.B.M., S.P.L., J.A.R. are cofounders of Epicore Biosystems Inc., which pursues commercialization of epifluidic devices. All other authors declare that they have no competing interests.

**This PDF file includes:**

Main Text
Figures 1 to 5

**Abstract**

Soft microfluidic systems that capture, store and perform biomarker analysis of microliter volumes of sweat, *in situ,* as it emerges from the surface of the skin, represent an emerging class of wearable technology with powerful capabilities that complement those of traditional biophysical sensing devices. Recent work establishes applications in real-time characterization of sweat dynamics and sweat chemistry in the context of sports performance and healthcare diagnostics. This paper presents a collection of advances in biochemical sensors and microfluidic designs that support multimodal operation in monitoring of physiological signatures directly correlated to physical and mental stresses. These wireless, battery-free, skin-interfaced devices combine, lateral flow immunoassays for cortisol, fluorometric assays for glucose and ascorbic acid (vitamin C), and digital tracking of skin galvanic responses. Systematic bench-top evaluations and field studies on human subjects highlight the key features of this platform for continuous, non-invasive monitoring of biochemical and biophysical correlates of stress state.

**Significance Statement**

Skin-interfaced, wireless devices for clinical-grade monitoring of physiological parameters are of growing interest for uses that range from delivering high quality care. This paper introduces a multifunctional skin-mounted microfluidic platform for capture and biomarker analysis of microliter of sweat that is a biofluid has potential relevance in biophysical sensing and healthcare. The focus is on colorimetric and digital assessments of a collection of parameters related to stress, including concentrations of vitamin C, cortisol and glucose in sweat, along with quantitative measurements of sweat rate and galvanic skin response. The results represent important additions to a portfolio of emerging capabilities in skin-interfaced technologies for physiological monitoring, with particular relevance to conditions that follow from unhealthy levels of physical and mental stress.

## Main Text

Soft, wearable microfluidic systems with capabilities in colorimetric, fluorometric and electrochemical sensing of sweat biomarkers offer a range of modalities for tracking performance, nutrition, wellness and health (1-5). These technologies exploit the rich mixture of solutes, metabolites, hormones of eccrine sweat and its non-invasive extraction directly from pores on the surface of the skin (6-10). A key requirement for the broad adoption of devices for sweat sensing is in contamination-free capture of precise volumes of sweat and *in situ* quantitative analysis of multiple biomarkers with relevance to muscle fatigue, dehydration, cystic fibrosis and others. An important and relatively unexplored frontier focuses on capabilities that support qualitatively expanded domains of application, such as those in tracking biochemical correlates of physical and mental stresses, and other aspects of cognitive status. This area represents the main focus of the results reported here.

Conventional techniques for sweat analysis rely on absorbent pads that adhere to the skin and require subsequent removal, special handling, bench-top centrifugation, and extraction of sweat for off-site analysis (11-13). These lab-based strategies are incompatible with real-time monitoring in field settings due to the need for expensive and bulky analysis equipment. Recent developments in advanced, soft forms of microfluidic technologies with integrated chemical and electrochemical sensors serve as the foundations for opportunities in real-time monitoring of various sweat biomarkers and tracking of sweat loss and local rate (3,14-16). Such devices are thin and flexible, thereby allowing conformal, water-tight coupling to the skin in clinical, athletic, and real-world environments. Related designs that incorporate capillary burst valves and mechanically reinforced stiffening materials (e.g. skeletal designs) enable time sequential analysis (i.e. chronosampling) of multiple sweat biomarkers, and application in demanding scenarios that involve physical impacts (17-19), respectively. In other demonstrations, surface coated electrodes with antibody- and enzyme-based assays capture information about cortisol and related biochemicals in a continuous mode of operation, although without field studies to demonstrate robustness of operation required for practical applications (20-23).

Simultaneous, reliable analysis of species such as cortisol, together with vitamin C and glucose, has the unique potential to yield insights into transient states of physical and mental stress. Cortisol release from the adrenal glands occurs in response to cognitive and physical stressors. This release activates the sympathetic nervous system (24) and triggers a complex chain of biochemical responses that lead to an increase in energy production (25). In particular, cortisol secretion in response to stress leads to elevated levels of glucose for muscle groups to consume in “fight or flight” scenarios. Increased cortisol levels over prolonged time periods, however, have been linked to conditions such as obesity, depression, hypertension, and diabetes (26).

Supplementary intake of vitamin C can counteract these harmful effects by boosting the immune response and attenuating cortisol levels (27). A desire to understand the complex relationship between cortisol, glucose, and vitamin C that define dynamic stress responses, motivates the development of devices for non-invasive monitoring of these stress-related biomarkers, as a means for establishing counteractive interventions.

This paper reports technologies that allow measurements of multiple stress-related biomarkers in battery-free, wireless skin-interfaced device platforms. The designs described here include skeletal microfluidic networks with integrated quantitative immunoassays for cortisol and fluorescence assays for glucose and vitamin C, along with features that allow for continuous sensing of sweat rate and conductivity using galvanic skin response (GSR). Demonstrations in bench-top studies and in field trials on human subjects highlight unique capabilities in multimodal and non-invasive monitoring of stress during exercise and at rest in real-world settings.

## Results and Discussion

**Soft, skin-interfaced skeletal microfluidic systems with lateral flow immunoassays and digital wireless measurement capabilities.** Skin interfaced systems with integrated immunoassays for sweat cortisol, fluorescent assays for glucose and ascorbic acid (vitamin C), and with electrochemical sensors, support an important range of capabilities for analysis of sweat biomarkers and sweat dynamics related to stress. These multimodal features in sensing exploit ruggedized microfluidic structures formed using a high modulus (~1 GPa), ultra-violet (UV) curable polyurethane (NOA81) embedded in a low modulus (~30 kPa; Ecoflex™, Smooth-On Inc., PA) silicone polymer matrix (28, 29). Fig. 1*A* shows an exploded view of this 'skeletal' microfluidic design. Compared to systems based on traditional elastomers, these polyurethane-based microfluidic structures greatly reduce the rate of evaporation of collected and stored sweat (29, 30) (*SI Appendix,* Fig. S1*A* and *B*) and serve as fluidic connections for embedded lateral flow immunoassays (LFIAs). *SI Appendix,* Fig. S1*C* and *D* shows a schematic illustration and an optical image of the skeletal microfluidic channels, respectively. The microfluidic channel stores ~ 70 μL, and electrodes within these channels establish contact with sweat for continuous, resistive measurements of sweat rate. Additional structures define micro-reservoirs and capillary burst valves for fluorescence-based measurements of glucose and ascorbic acid. A medical-grade skin adhesive layer with patterned openings attaches the device to the skin and defines access points for collection of sweat directly from skin pores, at positions aligned to inlets on the backside of the device (16). *SI Appendix,* Fig. S2 shows bench-top results of a device filling with artificial sweat at a rate of ~2 μL/min. An integrated system with electrodes, serpentine microchannels (600 μm width, 400 μm depth), and an LFIA for cortisol measurement appears in Fig. 1*B* and *C*. Fig. 1*D*

illustrates the design of the microfluidic assembly for fluorescence-based glucose and ascorbic acid assays.

Measurements of sweat loss and GSR exploit a collection of ultrathin electrodes (3-μm thick) defined photolithographically using a tacky formulation of polydimethylsiloxane (PDMS; 30:1 mixture of base to curing agent; Sylgard 184, Dow Corning; Midland, MI) as a temporary carrier. These patterned electrodes bond to the polyurethane in a UV curing process as shown in *SI Appendix,* Fig. S3*A*. *SI Appendix,* Fig. S3*B* presents images of electrodes after UV curing (top) and of a representative device with integrated electrodes (bottom). *SI Appendix,* Fig. S4 shows results from a simple peel test (Mark-10 ESM1500; ABQ Industrial L.P., TX; *SI Appendix*, Fig. S4*A-C*) that indicate levels of adhesion between the electrodes and the NOA81 substrate are ~6 times stronger than those associated with bonding to a tacky piece of PDMS (*SI Appendix,* Fig. S4*D* and *E*). Aligned bonding of the relief side of the prepared structure to the electrode layer yields an enclosed skeletal microfluidic channel system with integrated electrode interfaces (*SI Appendix,* Fig. S3*C*). The electrodes integrate along the serpentine microchannels with direct electrical interfaces to the sweat (Fig. 1*B*) as illustrated in *SI Appendix,* Fig. S5*A*. The system includes reference electrodes (① in *SI Appendix,* Fig. S5*A*), tracking electrodes (④ in *SI Appendix,* Fig. S5*A*), and a counter electrode (② or ③ in *SI Appendix,* Fig. S5*A*). *SI Appendix,* Fig. S5*B* shows magnified optical images of the reference (top) and tracking electrodes (bottom).

The packaging scheme highlighted in *SI Appendix,* Fig. S3*D* and *SI Appendix,* Fig. S6*A* involves steps to embed the microfluidic structure within silicone (Ecoflex™; 1:1 mixing, cured at room temperature for 12 h). A laser cutting process defines the perimeter of the resulting system (Fig. 1*E*, *SI Appendix,* Fig. S3*D, SI Appendix,* Fig. S7*B and* SI Note 1). Fig. 1*E* shows the device during mechanical twisting and bending. Fig. 1*F* and *SI Appendix,* Fig. S6*C-E* present results of finite element analysis (FEA) of the associated mechanics (SI Note 2). The serpentine geometries of the microfluidic channels and the low modulus, stretchable silicone matrix (~30 kPa) facilitate high levels of elastic deformations (31-33) (*SI Appendix,* Fig. S6*C-E*).

**Lateral flow immunoassay for cortisol.** The cortisol immunoassay relies on a competitive reaction that exploits anti-mouse-IgG (Anti-IgG) antibody, cortisol conjugated bovine serum albumin (cortisol-BSA) and gold nanoparticles (AuNPs; *SI Appendix,* Fig. S7*A*) with conjugated anti-cortisol antibodies (ACA) (34-36). *SI Appendix,* Fig. S7*B* and *C* schematically illustrates the reagents and immunoreactions. The ionic affinity of the hydrophobic surfaces of the AuNPs facilitates preparation of ACA-AuNP conjugates via spontaneous reaction of ACA and AuNP at ~ pH 7.2, ~23°C and 35% humidity. The immunoassay initiates as approximately 90% of collected

sweat (~60 μL) from the main channel reaches the conjugation pad, and cortisol in the sweat conjugates with the ACA-AuNP (cortisol-ACA-AuNP). Sweat then wicks along the nitrocellulose (NC) membrane to launch immunoreactions that occur along control and test lines defined on the membrane. The control line screens uncoupled ACA-AuNP by immobilizing the ACA active sites via cortisol-BSA. The test line senses cortisol-ACA-AuNP quantitatively as a result of binding to anti-IgG (34) (*SI Appendix,* Fig. S7*B* and *C*). Since there are multiple binding sites per AuNP, the sensitivity and dynamic range of the assay depend on the number of AuNPs, the number of binding sites per AuNP, the total amount of cortisol-BSA, and the concentration of sweat cortisol.

Fig. 2*A* highlights the zeta-potential as a function of ACA concentration (0.02, 0.2, 2 and 20 mg/mL ACA). The error bars are mean values across 3 samples with standard deviations for each concentration condition for conjugation of AuNPs (diameters of 30 nm, with highest optical density at ~550 nm wavelength) as shown in *SI Appendix* Fig. S7*A*. Increasing the concentration of ACA increases the surface charge, until saturation at ~2 mg/mL ACA. These measurements indicate that ~0.5 mg/mL ACA (~ -20 mV of zeta-potential) is a good choice for conjugation of ACA and AuNPs (37, 38). Fig. 2*B* shows the absorbance spectrum for ACA-AuNP samples for various times of conjugation. The results reveal the time dependence of AuNP aggregation, and the corresponding time required for saturation of the color response (39, 40) (*SI Appendix,* Fig. S8*A*). Insufficient conjugation time produces samples with absorbance lower than those processed in an optimized manner (3 min, as in Fig. 2*B*). Fig. 2*C* shows that the peak absorbance occurs at ~280 nm, a wavelength range where aromatic groups in the amino acid residues and antibodies absorb strongly (40-42). Transmission electron microscope (TEM) images (*SI Appendix,* Fig. S8*B*) compare AuNPs before (left) and after conjugation (right), and the image after conjugation (right) shows development of ACA on the AuNP surface. *SI Appendix,* Fig. S8*C* shows the effects of physiologically relevant changes in sweat pH (pH 5.0, 6.0, 7.0 and 8.0) on zeta-potentials for samples of ~0.5 mg/mL ACA conjugated with 30-nm AuNP. The shift in zeta-potentials is ~ -25 mV to ~ -41 mV for changes in pH from 5.0 to 8.0 that is based on that the carboxyl groups and hydroxyl groups are ionized in the shifting alkaline condition (43).

The lateral flow strip consists of a conjugation pad (Glass fiber; GFB-R7L; mdi Membrane Technologies, Inc., PA; *SI Appendix,* Fig. S9*A*) and a NC membrane (10-μm pore size) with color development at the cortisol-BSA control line (*SI Appendix*, Fig. S9*B*). The absorbent pad confines the reaction system within the NC membrane to ensure rapid and accurate immunoassay reactions. Selection of the membrane material and pore size follow considerations based on the Lucas-Washburn model, according to (44, 45);

$$L^2 = \gamma r t \cos\theta \,/\, 2\eta \qquad \text{(Eq. 1)},$$

where $L$ is the absorption distance, $\gamma$ is the surface tension, $r$ is the pore radius, $\theta$ is the contact angle between the membrane material and the solution, $t$ is the time and $\eta$ is the dynamic viscosity of the solution. Once the collected sweat activates LFIA reaction from conjugation pad, the overall reaction time remains constant, consistent with the Lucas-Washburn model and independent of sweat rate. *SI Appendix,* Fig. S9*C-E* show the process for assembly of the LFIA strip and optical images before and after laser cutting. A dispensing process delivers cortisol-BSA and anti-IgG to the control and test lines, respectively. The immunoassay design and detection range depend on the amount of immobilized cortisol-BSA on the control line and the active surface areas of both the control and test lines. Color development tests on the control line as a function of concentration of cortisol-BSA determine the optimal quantity of cortisol-BSA (Fig. 2*D*). Fig. 2*D* shows the onset of color saturation at ~7 mg/mL cortisol-BSA with the assembled test strip (rectangular; 5 cm x 0.5 cm) that 1 mL of prepared 0.8 OD ACA-AuNP is added to the unprocessed conjugation pad (*SI Appendix,* Fig. S9*D*; 6 cm x 1 cm of glass fiber) in the assembly process. Accurate colorimetric evaluation of the LFIA involves analysis of images captured with a smartphone, after correcting for ambient lighting conditions (e.g. direct sun light, shade, indoor lighting, transmission properties through the polyurethane micro-channel; Eq. S1) and with the NC membrane surface as a white reference (SI Note 3) (5, 46).

Fig. 2*E* shows an image of completed LFIA strip and *SI Appendix,* Fig. S10*A* shows the strip integrated in a device for measurements across the physiological range of cortisol concentrations at the test line (Fig. 2*F*; 5, 10, 30, 60 and 100 ng/mL; 50 µg/mL Anti-IgG immobilized at the test line). Pictures of the LFIA strips after 10 min of color development appear in *SI Appendix,* Fig. S10*B*. Tests with volunteer subjects indicate the ability to measure cortisol concentrations accurately using this approach, as an alternative to enzyme-linked immunosorbent assay (ELISA) tests that is reliable bench-top cortisol assay, as shown in Fig. 2*G* (47).

**Fluorescence-based assays for glucose and ascorbic acid.** The device also supports fluorescence-based assays for glucose and ascorbic acid. A pair of reservoirs connected by microchannels and capillary burst valves enable time-sequential sampling of sweat for these measurements. The passive valve geometries have lateral dimensions (~50 µm) that are significantly smaller than those of the microchannels leading into the reservoirs (150 µm). The burst pressure mechanism follows from the Laplace-Young equation (Eq. 2) according to:

$$\text{Burst Pressure} = -2\sigma\left[\frac{cos\theta_I^*}{b} + \frac{cos\theta_A}{h}\right] \qquad \text{(Eq. 2)}$$

where $\sigma$ is the surface tension of liquid, $\theta_A$ is the contact angle of the channel, $\theta_I^*$ is the min [$\theta_A$+ $\beta$; 180˚], $\beta$ is the diverging angle of the channel, $b$ and $h$ are the width and the height of the diverging

section, respectively (30, 48, 49). *SI Appendix*, Fig. S11*A* illustrates the overall design of this network of channels, assays, and the capillary burst valves where 'Valve#1' and 'Valve#2' have diverging angles of 90˚ and 120˚, respectively. Magnified optical images for the valves are shown in *SI Appendix*, Fig. S11*B*. Tailoring the burst pressures for these valves ensures ordered routing of sweat as it fills into the reservoirs. A separate set of circular reservoirs not connected to the microfluidic network serve as fluorescence reference markers prefilled with fluorescent dye (5 mg/mL Tetramethylrhodamine, Ethyl Ester, Pechlorate; TMRE; Thermo Fisher Scientific, Waltham, MA) (50).

*SI Appendix*, Fig. S12*A* and *B* summarize reactions that involve glucose and ascorbic acid with glucose oxidase (GOx) and ascorbic acid oxidase (AOx) enzymes, respectively. The oxidation reactions for both substrates generate hydrogen peroxide, and excess activity of horseradish peroxidase (HRP) leads to reduction of a fluorometric probe (OxiRed$^{TM}$) to form resorufin as the basis for a fluorescence signal (Fig. 3*A*; $\lambda_{excitation}$: ~550 nm wavelength and $\lambda_{emission}$: ~600 nm wavelength) with magnitude that depends on the concentration (51) (*SI Appendix*, Fig. S12*C*). SI Note 4 summarizes the details of enzymes preparation for glucose and ascorbic acid assays. *SI Appendix*, Fig. S12*D* and *E* shows the effect of pH on the activity of GOx and AOx, respectively. An apparatus with integrated excitation and emission filters attaches to a smartphone to facilitate rapid measurement of the fluorescence *in situ* (49) (Fig. 3*B*). The emission filter passes only light with wavelengths longer than 610 nm. *SI Appendix*, Fig. S12*F* shows the key features of this module and its coupling to a smartphone imager. This setup facilitates capture of fluorescence signals, as measures of the concentration of target substrates (*i.e.* glucose and ascorbic acid). Fig. 3*C* features signals from glucose and ascorbic acid relative to those from the TMRE reference reservoir. Calibration involves first analyzing the signal intensity from each reservoir and then normalizing these results by the intensity of TMRE (49, 52) (Eq. S2). The depth of each microreservoir controls the dynamic range of the fluorescence signal, according to the Beer-Lambert law (53). Fig. 3*D* shows the effect of the silicone packaging on the fluorescent signal at 0:10, 1:9, 3:7 and 10:0 ratios (0%, 10%, 30% and 100%, respectively) of black and white pigments mixed in uncured Ecoflex at ~5% (w/w). Fig. 3*E* and *F* exhibit examples that the fluorescence intensity increases for glucose and ascorbic acid assays in a linear manner with relevant range of concentrations.

**Battery-free, wireless electronic interface for readout of sweat rate and galvanic skin response.** Fig. 4*A* highlights the wireless electronic module, which consists of three electrodes (sweat rate, skin conductance, and sweat reference), a near field communication (NFC) microcontroller (RF430, ISO/IEC 15693, ISO/IEC 18000-3; Texas Instruments, Dallas, TX) and an

RF antenna. The microcontroller receives power wirelessly (*SI Appendix*, Fig. S13*A*-*D*) from an NFC-enabled device such as smartphone (16, 54, 55). The electrodes deliver alternating current (AC) to the skin to measure galvanic skin response (GSR), with a common node of $V_{TMS}$ for applying an AC driving signal (Fig. 4*B* and *C*; $R_a$, $R_b$ and $R_c$ for 100 kΩ, 300 kΩ and 10 kΩ, respectively). The digital readout system compares measured resistances to known reference resistors, $R_a$ $R_b$ and $R_c$ to allow for evaluating sweat rate, GSR and sweat conductivity, respectively (Fig. 4*C*). The analog to digital converter (ADC) ports on the NFC microcontroller (RF430, ISO15693 interface) acquire data from the three electrodes of $R_L$, $R_G$ and $R_R$ (Fig. 4*C*). The ADC output voltages for each channel can be described by the following equations:

$$\mathrm{ADC0} = V_{TMS} \times \frac{R_a}{R_a+R_L} - V_f,\ \mathrm{ADC1} = V_{TMS} \times \frac{R_b}{R_b+R_G} - V_f,\ \mathrm{ADC2} = V_{TMS} \times \frac{R_c}{R_c+R_R} - V_f \quad \text{(Eq. 3)}$$

where $R_L$ is the resistance across the pair of electrodes in main channel, $R_G$ is the resistance across the electrodes for GSR, $R_R$ is the resistance at the reference electrode and $V_f$ is the forward voltage of the rectifier (~150 mV) (16). Fig. 4*D* shows the terminals for GSR (left; *SI Appendix*, Fig. S13*E*) and the tracking and reference electrodes that couple with the embedded electrodes in microfluidic channel (right). The acquired data passes wirelessly to the smartphone. *SI Appendix*, Fig. S13*F* provides details on the individual terminals of the RF430 and TSV632 and the layer of PDMS that prevents ingress of external moisture, respectively.

*SI Appendix*, Fig. S14*A* summarizes conductance measurements from ADC0 for artificial sweat collected in the main microchannel for various electrolyte concentrations. The captured sweat volume depends linearly on sweat filling length along the channel (*SI Appendix*, Fig. S6*A*) and, as a result, on the resistance at the tracking electrodes according to:

$$L = \alpha \cdot R_R/R_L \quad \text{(Eq. 4)}$$

where $L$ is the filling length ($L$ = 0-165 mm) and $\alpha$ is a coefficient that accounts for the ratio of the lengths of the reference and tracking electrodes (reference electrode: 1.5 mm; tracking electrodes: 165 mm). Measurements at 1 kHz minimize the dependence of impedance phase on the conductivity of the skin and sweat (16) (*SI Appendix*, Fig. S14*B*-*D*). Bench-top and field testing with volunteer subjects determine the relationship between ADC2 and sweat conductivity (*SI Appendix*, Fig. S14*E* and Fig. 4*E* for bench-top and field testing, respectively).

Evaluations of skin conductivity using the GSR electrodes, as shown in *SI Appendix*, Fig. S13*E* and comparison with sweat rate provide important insights into sweat gland activity, including sweat rate and ion reabsorption. Coupling of electronics module with the skeletal microfluidics electronically enables sweat rate data collecting. The magnets (3-mm diameter, ~0.5-mm thickness), attached to the electronics module, offer robust magnetic forces for mechanical coupling

with the electrode terminals (16) (Fig. 1*A* and *SI Appendix*, Fig. S14*F*). Previous studies demonstrate that sweat electrolyte concentrations increase with increasing sweat rate (55-57). Prolonged exercise on a stationary bike induces high sweat rates, which could give rise to ion reabsorption. Fig. 4*F* shows results that correlate ΔGSR with skin temperature for the initial phases of exercise (~10 min at 18°C room temperature). A warmup period of 10-15 min leads to sweating and development of a stable skin temperature (58). Fig. 4*G* shows representative ΔGSR data collected from the forearm of a subject. The eccrine glands selectively reabsorb ions, especially sodium, during sweating as the basis of physiological regulation for homeostasis. The constant ΔGSR trend shown in Fig. 4*G* reflects this type of physiological regulation at low sweat rate phase of under ~0.8 μL/min. Further exercise without hydration induces over-perspiration and perturbs the regulation system. The ΔGSR data is consistent with this behavior, as it increases after 0.7 μL/min sweat rate as the ion resorption rate exceeds the excretion rate (59-62) (Fig. 4*G*).

**Demonstrations and field testing.** Field tests illustrate capabilities in measurement of cortisol, glucose and ascorbic acid along with digital tracking of sweat rate and GSR through studies with four healthy volunteer subjects engaged in physical exercise on a stationary bike in a gym environment (*SI Appendix*, Fig. S15*A*-*C*; 18-22°C temperature and 15-30% humidity). The initial set of experiments involve data collection from subjects #1 and #2 in the morning and evening. Sweating was induced within 30 min after the subject woke up at ~7am and before going to sleep around 7pm (Fig. 5*A* and *B*). Intensive work periods ensued for ~7 days (including working overnight for several days with consumption of caffeine) and rest (regular patterns of sleeping and meals) for 14 days, serving as short-term stressors. Additional short-term studies with subjects #3 and #4 focused on cortisol, glucose and ascorbic acid measurements along with measurements of sweat rate and GSR (Fig. 5*C*-*J*) in the morning and evening during intensive work, rest with healthy diet, and control (63-65).

*SI Appendix,* Fig. S16 shows these sequences of events and methods for capturing sweat information at each stage using a smartphone. The filling of sweat into the microchannels activates the glucose and ascorbic acid assays within ~10-15 min after the start of the stationary bike exercise. Upon filling of the reservoirs for glucose and ascorbic acid assays, a smartphone camera with the shielding module (Fig. 3*B* and *SI Appendix*, Fig. S12*F*) captures the fluorescent signals. As sweat fills into the main channel, measurements of sweat rate and GSR (4~13 separate times) can be performed by placing the smartphone in proximity to the device. The LFIA assay activates after complete filling of the main channel (~70 μL). The digital camera on the smartphone captures the developed color.

374 Fig. 5*A*-*D* compares measurements of cortisol conducted with the LFIA and a bench-top
375 ELISA protocol in the morning and evening, under intensive work and resting conditions. Under
376 ordinary, routine circumstances, diurnal variations of cortisol level among the subjects exhibit
377 standard patterns, with concentrations that peak in the morning, to facilitate focus during the
378 daytime, and then gradually decrease through the afternoon and evening. This cortisol circadian
379 rhythm is apparent in data from subjects #3 and #4, as shown in Fig. 5*C* and *D* (64, 65). The
380 subjects, during intensive work, experience physiological stress, fatigue and irregular life patterns
381 with inadequate sleep. These conditions disrupt the cortisol-melatonin circadian rhythm. As a
382 result, the hypothalamus region of the brain produces corticotropin releasing hormone (CRH),
383 which in turn, activates the hypothalamic-pituitary-adrenal axis and stimulates anterior pituitary
384 activity (23, 24, 66), thereby increasing cortisol production and disrupting of cortisol circadian
385 rhythm (67). The cortisol levels for Subject #2, #3 and #4 during intensive work show disruptions
386 of circadian rhythm, consistent with physiological conditions that reflect exhaustion (Fig. 5*B* and *C*).
387 This disruption could aggravate the psychological state (e.g. anxiety, insomnia, etc.). Fig. 5*K*
388 demonstrates the accuracy and reliability of the LFIA in the device compared with bench-top ELISA
389 results ($R^2$=0.7974). The control tests measuring saliva cortisol levels before and after exercise
390 show that the effect of exercise intensity on cortisol level is small (68) compared to circadian rhythm
391 changes that occur during the day. After intense work condition, the subjects return to a routine
392 life pattern for 2 weeks and consume ascorbic acid (1000 mg per a day for subject #3 and #4) (69).
393 The result is that the cortisol patterns recover to normal circadian rhythm, as shown in Fig. 5*A*-*C*.
394 Although subjects #1-#3 show lower cortisol levels after 14 days, the relative changes in sweat
395 cortisol levels due to circadian rhythm appear to dominate compared to dietary interventions for
396 subject #4 (Fig. 5*D*). Fig. 5*E* and *F* show that the ascorbic acid levels increase from ~0 μM to ~0.33
397 μM for subject #3 and from ~0 μM to ~0.42 μM for subject #4, as a result of vitamin C intake. By
398 contrast, the glucose levels exhibit no specific trends, i.e. ~0.62 μM and ~0.80 μM for subject #3
399 and 0.84 μM and 0.81 μM for subject #4, as mean values of measurements taken on day 0 and
400 day 14. *SI Appendix*, Fig. S15*D* and *E* show glucose and ascorbic acid measurements at day 0,
401 2, 6, 10 and 14 for these same two subjects. These results show that the device along with
402 integrated assays have practical utility, as the glucose and ascorbic acid sensitivity ranges are
403 within previously reported physiological ranges (3, 70).

404 Representative results for sweat rate and ΔGSR appear in Fig. 5*I*-*J*. These findings
405 establish correlations between ΔGSR and sweat rate, likely associated with resorption and
406 secretion of ions due to sweating. Sweat rate measurements from Subjects #1 and #2 appear in
407 Fig. 5*H* and *I*, with comparisons to ΔGSR in *SI Appendix*, Fig. S15*F* and *G*. Wirelessly acquired
408 data from ADC0 and ADC2 yield the sweat rate and electrolyte concentrations, respectively.
409 Comparisons of ΔGSR and sweat rate in Fig. 5*I* and *J* suggest that resorption behavior occurs for

secreted ions (i.e. sodium) from the proximal secretory coil (18, 59, 70-72). In the limiting case, the rate of secretion of ions exceeds the rate of resorption, thereby leading to an increase in ΔGSR at a critical sweat rate (73-74). Fig. 5*I* and *J* shows that ΔGSR measurements for subjects #3 and #4 remain steady until the sweat rate reaches ~1.1 μL/min for subject#3 and ~0.8 μL/min for subject #4, at which point the ΔGSR increases.

## Conclusion

Eccrine sweat is an interesting, yet incompletely understood, class of biofluid that contains a range of chemical species whose concentrations could provide significant information on physiological status. The potential relevance spans sports science, diagnosis in clinical medicine and evaluations of military readiness. The multifunctional device platform described here exploits a soft microfluidic network of hard channels and reservoirs, with integrated flexible electronic systems, as a practical lab-on-a-chip type system with immunoassays, fluorometric detection capabilities and wireless functionality tailored specifically to monitoring of physical and mental stresses. A key feature is the lateral flow integration for immunoassay analysis of sweat cortisol. The fluorescence assay provides information on other trace substrates such as glucose and ascorbic acid. Wireless modes of operation based on NFC protocols support real-time, wireless digital tracking of sweat rate and GSR. Field tests on human subjects engaged in activities to create and then relieve stresses demonstrate the utility of the technology in this important context, as well as its ability to address scenarios of practical interest. The versatile design principles introduced here can be configured to address many additional capabilities in sweat collection, storage and chemical analysis in remote field settings (e.g. modified skin mounted microfluidics, in which micro-photodetector and excitation light are embedded to enable FL readouts).

## Materials and Methods

**Fabrication of soft skeletal microfluidics with flexible electrodes system.** Fabrication began with the formation of a mold from a silicon wafer patterned using photolithography techniques. More precisely, photoresist KMPR1010 was spin-cast on a silicon wafer at 3000 rpm for 30 s, baked on a hot plate at 110°C for 3 min, exposed to UV irradiance at 300 $mJ \cdot cm^{-2}$ for 2 min and developed with developer MF917. Deep reactive-ion etching (polymethylmethacrylate coating; STS Pegasus ICP-DRIE, SPTS Technologies Ltd, UK) removed the exposed silicon to a selected depth (~400 μm). A prepolymer to polydimethylsiloxane (PDMS; Sylgard 184, Dow Corning, Midland, MI, mixed at a 10:1 ratio of base to curing agent by weight) was then cast and cured on the silicon structures to yield soft molds. These molds were used to form structures of NOA (Norland Optical Adhesive;

NOA 81, Norland Products, Inc., Cranbury, NJ; Partial curing; Expose to 30 W UV light for 4~10 min; *SI Appendix*, Fig. S1*B*).

Fabrication of Cu electrodes relied on a photolithographic process, whereby photoresist (AZ4620) was spin-cast at 3000 rpm for 30 s, and then baked on a hot plate at 60°C for 1 min. After UV irradiance at 300 $mJ \cdot cm^{-2}$ to expose the photoresist, a development process for 1 min yielded the desired pattern. Next, wet etching with copper etchant (HFCE100, Transense, Oxfordshire, UK) of Cu foils (DuPont, Wilmington, DE) laminated onto glass slides (Fisherbrand, Pittsburgh) coated with PDMS (Sylgard 184, Dow Corning, Midland, MI; mixed at a 20:1 ratio of base to curing agent by weight and partially cured on a hot plate at 110°C for 3 min; *SI Appendix*, Fig. S3*A*) removed the exposed regions of the Cu. Casting a ~500 μm thick layer of NOA 81 on the patterned Cu-PDMS substrate and exposing to UV light (30 W for 4 min) enabled transfer of the Cu electrodes to the surface of the NOA 81 (*SI Appendix*, Fig. S3*A*). Assembly of NOA microfluidic trenches (*SI Appendix*, Fig. S1*D*) and electrodes (*SI Appendix*, Fig. S3*B*) exploited uncured NOA81 to create sealed channels with precise alignment (*SI Appendix*, Fig. S3*C*). A laser cutter (ProtoLaser R; LPKR, Germany) defined the perimeter of the assembly as the final step to complete the fabrication. SI Note 4

**Lateral flow immunoassay platform preparation.** The addition of 1 M NaOH to colloidal 30-nm gold nanoparticles (GNP; Sigma-Aldrich, St. Louis, MO) shifted the pH close to 7.0. Adding 0.5 mg/mL anti-cortisol antibody (ACA; ab1951, Abcam Inc, Cambridge, UK) to a final concentration of ~0.5 μg/mL and incubating (rotating at 30 rpm) the solution for 1, 3, 20 min enabled spontaneous conjugation of antibody onto the activated GNP. Adding 10% (w/v) Bovine serum albumin (BSA; to final concentration of 0.1%; Sigma, St. Louis, MO), allowing stabilization at room temperature for 1 h, centrifuging (9000 g for 30 min at 4 °C, followed by ~4 times repetition of washing-resuspending of precipitated pellet with a storage buffer; PBS buffer includes 1% BSA and 2% sucrose) and drying of the separated precipitation at room temperature for 4 h yielded anti-cortisol antibody conjugated gold nanoparticles (ACA-GNP; stored at 4°C).

Cortisol-BSA and IgG antibody were immobilized on a nitrocellulose membrane (pore size: 5, 8, 10, 12, 15 μm; Advanced Microdevices, Ambala Cantt, India) as the control and test lines, respectively (Claremont BioSolutions, LLC, CA). A sample-conjugation pad (Advanced Microdevices, Ambala Cantt, India) was saturated with ACA-GNP for 1 h and then dried for 30 min at 37 °C. The prepared nitrocellulose membrane and an absorbent pad (Filter paper No.1, Whatman, GE Healthcare Life Sciences, UK), as shown in *SI Appendix*, Fig. S9*C*, served as supports for the lateral flow immunoassay. Standard protocols for ACA, Cortisol-BSA, IgG antibody and BSA set a 1-year shelf life from when the package is delivered.

**Electronics design and assembly.** Fabrication began with patterning of a two-layer printed circuit board by processing of multilayer foils of Cu-PI-Cu (18 μm/75 μm/18 μm) with a UV laser cutter (ProtoLaser U4; LPKF, Germany). The main processor, RF430FRL152HCRGER (RF430, ISO/IEC 15693, ISO/IEC 18000-3; Texas Instruments, Dallas, TX) served as the NFC platform, with the ability to rectify incident power from a smartphone device at up to 720 μW at 2.0 V, depending on coupling efficiency, and relaying data over the 13.56 MHz communications link. The RF430 supports 14-bit Sigma-Delta ADC with triple analog inputs at an input range up to 900 mV and maximum sampling frequency of 2 kHz, down-sampled to 1 Hz resolution. Signal amplification and measurement of the main and reference channels used another chip, TSV634QFN16 (STMircoelectronics, Geneva, Switzerland), as a four-channel operation amplifier with low energy consumption (60 μA at 5V) and large unity gain-bandwidth (800 kHz). On power-up, the system sourced a 5 kHz, rail-to-rail square wave to the channels, causing an AC current to flow through the collected sweat. The magnitude of this current is proportional to the concentration of ions in sweat, as an electrical impedance that causes the sourced 5 kHz waveform to attenuate during passage through the sweat. This attenuation reduces the amplitude of the waveform whose rectified voltage is buffered and measured by the TSV634 and ADC, respectively. This rectified voltage level is sampled, processed, and relayed to an NFC compatible reader by the RF430. An NFC-compatible smartphone (LG Nexus 5X; LG, Seoul, South Korea) and custom-developed application for the Android operating system enabled visualization of the data.

**Field studies.** Field studies with four healthy volunteers who exercise regularly involved operating stationary bike in gym environment (18-20°C temperature and 15-30% humidity) before, during and after intensive works. The intensive works involve mostly the environment of mental stress (i.e. long studying or research time with irregular sleeping pattern) that is followed by ascorbic acid supplement of 1,000 mg/day for the next 14 days (75). All subjects provided signed consent, and had medical consultations before and after field tests with a medical doctor. This study was approved by the Institutional Review Board (IRB: STU00208494) at Northwestern University. Control tests using saliva from the subjects verified circadian rhythm changes observed in sweat cortisol levels. Prior to mounting the devices, the skin was cleaned with 70% ethanol. Subjects wore sportswear (shorts and t-shirt) for the tests.

**Acknowledgments**

J.K. acknowledges the support from National Research Foundation of Korea (NRF-2020R1F1A1068083). R.G., A.J.A., and J.B.M. acknowledge funding support from the Leo Science

& Tech Hub. S.H.S. acknowledges the support from the Primary Research Program (20A01021) of the Korea Electrotechnology Research Institute. This work utilized Northwestern University Micro/Nano Fabrication Facility (NUFAB), which was partially supported by Soft and Hybrid Nanotechnology Experimental (SHyNE) Resource (NSF ECCS-1542205).

## References

1. M. Bariya, H. Y. Y. Nyeln, A. Javey, Wearable sweat sensors. *Nat. Electron.* 1, 160-171 (2018).
2. T. R. Ray *et al*., Bio-integrated wearable systems: A comprehensive review. *Chem. Rev.* 119, 5461-5533 (2019).
3. J. Choi *et al*., Soft, skin-integrated multifunctional microfluidic systems for accurate colorimetric analysis of sweat biomarkers and temperature. *ACS Sens.* **4,** 379-388 (2019).
4. J. T. Reeder *et al*., Waterproof, electronics-enabled, epidermal microfluidic devices for sweat collection, biomarker analysis, and thermography in aquatic settings. *Sci. Adv.* **5,** eaau6356 (2019).
5. S. B. Kim *et al*., Super-absorbent polymer valves and colorimetric chemistries for time-sequenced discrete sampling and chloride analysis of sweat via skin-mounted soft microfluidics. *Small* **14,** 1703334 (2018).
6. K. Sato, The physiology, pharmacology, and biochemistry of the eccrine sweat gland. *Rev. Physiol. Biochem. Pharmacol.* **79,** 51-131 (1977).
7. A. P. Jones, L. M. C. Webb, A. O. Anderson, E. J. Leonardo, A. Rot, Normal human sweat contains interleukin-8. *J. Leukoc. Biol.* **57,** 434-437 (1995).
8. G. Cizza *et al*., Elevated neuroimmune biomarkers in sweat patches and plasma of premenopausal women with major depressive disorder in remission: the POWER study. *Biol. Psychiatry* **64,** 907-911 (2008).
9. A. Mena-Bravo, L. De Castro, Sweat: a sample with limited present applications and promising future in metabolomics. *J. Pharm. Biomed. Anal.* **90,** 139-147 (2014).
10. M. D. Hladek *et al*., Using sweat to measure cytokines in older adults compared to younger adults: a pilot study. *J. Immunol. Methods* **454,** 1-5 (2018).
11. N. Hamouti *et al*., Sweat sodium concentration during exercise in the heat in aerobically trained and untrained humans. *Eur. J. Appl. Physiol.* **111,** 2873-2881 (2011).
12. Y. Inoue, M. Nakao, H. Ishizashi, J. Tsujita, T. Araki, Regional differences in the $Na^+$ reabsorption of sweat glands. *Appl. Human Sci.* **17,** 219-221 (1998).
13. T. Araki, K. Matsushita, K. Umeno, A. Tsujino, Y. Toda, Effect of physical training on exercise-induced sweating in women. *J. Appl. Physiol.* **51,** 1526-1532 (1981).
14. A. J. Bandodkar *et al*., Soft, skin-interfaced microfluidic systems with passive galvanic stopw

553 atches for precise chronometric sampling of sweat. *Adv. Mater.* **31,** 1902109 (2019).
554 15. J. T. Reeder *et al.,* Resettable skin interfaced microfluidic sweat collection devices with
555 chemesthetic hydration feedback. *Nat. Commun.* **10,** 1-12 (2019).
556 16. S. B. Kim *et al*., Soft, skin-interfaced microfluidic system with wireless, battery-free electronic
557 s for digital, real-time tracking of sweat loss and electrolyte composition. *Small* **14,** 1802876
558 (2018).
559 17. L. B. Baker, R. P. Nuccio, A.E. Jeukendrup, Acute effects of dietary constituents on motor skil
560 l and cognitive performance in athletes. *Nutr. Rev.* **72,** 790-802 (2014).
561 18. B. Murray, Hydration and physical performance. *J. Am. Coll. Nutr.* **26,** 542S-548S (2007).
562 19. D.L. Fogt *et al.,* Hydration status of air force military basic trainees after implementation of th
563 e back-mounted hydration system. *Mil. Med.* **174,** 821-827 (2009).
564 20. W. Gao *et al*., Fully integrated wearable sensor arrays for multiplexed *in situ* perspiration ana
565 lysis. *Nature* **529,** 509-514 (2016).
566 21. H. Y. Y. Nyein, *et al.* A wearable electrochemical platform for noninvasive simultaneous
567 monitoring of $Ca^{2+}$ and pH. *ACS Nano* **10,** 7216-7224 (2016).
568 22. R. M. Torrente-Rodríguez, *et al.* Investigation of cortisol dynamics in human sweat using a
569 graphene-based wireless mHealth system. *Matter* 2, 921-937 (2020).
570 23. J. R. Sempionatto *et al.*, Epidermal enzymatic biosensors for sweat vitamin C: Toward
571 personalized nutrition. *ACS Sens.* **5**, 1804-1813 (2020).
572 24. P. Monteleone *et al.,* Temporal relationship between melatonin and cortisol responses to
573 nighttime physical stress in humans. *Psychoneuroendocrinology* **17**, 81-86 (1992).
574 25. M. M. Landys, M. Ramenofsky, J. C. Wingfield, Actions of glucocorticoids at a seasonal
575 baseline as compared to stress-related levels in the regulation of periodic life processes. *Gen.*
576 *Comp. Endocrinol.* **148**, 132-149 (2006).
577 26. J. Gordon Betts et al., “Chapter 17.6 The adrenal glands” in Anatomy and physiology. *BCcam*
578 *pus*, Victoria, BC Canada (2020). Retrieved from https://opentextbc.ca/anatomyandphysiolog
579 y/chapter/17-6-the-adrenal-glands/. July 15, 2020.
580 27. A. D. L. Roberts, S. Wessely, T. Chalder, A. Papadopoulos, A. J. Cleare, Salivary cortisol
581 response to awakening in chronic fatigue syndrome. *Br. J. Psychiatry* **184**, 136-141 (2004).
582 28. H. Mai, R. Mutlu, C. Tawk, G. Alici, V. Sencadas, Ultra-stretchable MWCNT-ecoflex
583 piezoresistive sensors for human motion detection applications. *Compos. Sci. Technol.* **173,**
584 118-124 (2019).
585 29. J. Choi, *et al*., Skin-Interfaced Microfluidic Systems that Combine Hard and Soft Materials fo
586 r Demanding Applications in Sweat Capture and Analysis. *Adv. Healthc. Mater*. **19**, 2000722
587 (2020).
588 30. S. B. Kim *et al.,* Soft, skin-interfaced microfluidic systems with integrated enzymatic assays f

589 or measuring the concentration of ammonia and ethanol in sweat. *Lab Chip* **20,** 84-92 (2020).
590 31. A. Koh *et al*., A soft, wearable microfluidic device for the capture, storage, and colorimetric se
591 nsing of sweat. *Sci. Transl. Med.* **8,** 1-13 (2016).
592 32. D.-H. Kim *et al.,* Epidermal electronics. *Science* **33,** 838-843 (2011).
593 33. Y. Liu *et al*., Epidermal mechano-acoustic sensing electronics for cardiovascular diagnostics
594 and human-machine interfaces. *Sci. Adv.* **2,** e1601185 (2016).
595 34. W. Leung et al., One-step quantitative cortisol dipstick with proportional reading. *J. Immunol.*
596 *Methods* **281,** 109-118 (2003).
597 35. S. Choi *et al*., Real-time measurement of human salivary cortisol for the assessment of psych
598 ological stress using a smartphone. *Sens. Biosensing Res.* **2,** 8-11 (2014).
599 36. S. Choi, J.-H. Lee, J.-S. Choi, H.-I. Jung, Economical and rapid manufacturing of lateral flow i
600 mmunosensor using fountain pens and gold colloidal solution. *Anal. Methods* **7,** 1834-1842 (2
601 015).
602 37. R. Del Caño *et al.,* Hemoglobin bioconjugates with surface-protected gold nanoparticles in
603 aqueous media: the stability depends on solution pH and protein properties. *J. Colloid*
604 *Interface Sci.* **505,** 1165-1171 (2017).
605 38. C. Garcia-Hernandez, A. K. Freese, M. L. Rodriguez-Mendez, A. K. Wanekaya, *In situ* synthe
606 sis, stabilization and activity of protein-modified gold nanoparticles for biological applications.
607 *Biomater. Sci.* **7,** 2511-2519 (2019).
608 39. I. V. Safenkova, E. S. Slutskaya, V. G. Panferov, A. V. Zherdev, B. B. Dzantiev, Complex
609 analysis of concentrated antibody-gold nanoparticle conjugates' mixtures using asymmetric
610 flow field-flow fractionation. *J. Chromatogr. A* **1477,** 56-63 (2016).
611 40. R. Marega *et al*., Antibody-functionalized polymer-coated gold nanoparticles targeting cancer
612 cells: an invitro and in vivo study. *J. Mater. Chem*. **22**, 21305 (2012).
613 41. Y. Cui, Y. Wang, W. Hui, Z. Zhang, X. Xin, C. Chen, The synthesis of goldmag nano-particles
614 and their application for antibody immobilization. *Biomed. Microdevices* **7**, 153-156 (2005).
615 42. S. Xiulan, Z. Xiaolian, T. Jian, J. Zhou, F. S. Chu, Preparation of gold-labeled antibody probe
616 and its use in immunochromatography assay for detection of aflatoxin B1. *Int. J. Food*
617 *Microbiol.* **99**, 185-194 (2005).
618 43. P. Xu, H Wang, R. Tong, G. Du, W. Zhong, Preparation and morphology of $SiO_2$/PMMA nano
619 hybrids by microemulsion polymerization. *Colloid. Polym. Sci.* **284**, 755-762 (2006).
620 44. D. Gasperino, T. Baughman, H. V. Hsieh, D. Bell, B. H. Weigl, Improving lateral flow assay pe
621 rformance using computational modeling. *Annu. Rev. Anal. Chem.* **11,** 219-244 (2018).
622 45. E. W. Washburn, The dynamics of capillary flow. *Phys. Rev*. **17**, 273 (1921).
623 46. H. Araki *et al*., Materials and device designs for an epidermal UV colorimetric dosimeter with
624 near field communication capabilities. *Adv. Funct. Mater.* **27,** 1604465 (2017).

47. M. Shimada et al., Determination of salivary cortisol by ELISA and its application to the assessment of the circadian rhythm in children. *Horm. Res.* **44**, 213-217 (1995).
48. J. Choi, D. Kang, S. Han, S. B. Kim, J. A. Rogers, Thin, soft, skin-mounted microfluidic networks with capillary bursting valves for chrono-sampling of sweat. *Adv. Healthc. Mater.* **6,** 1601355 (2017).
49. Y. Sekine *et al.*, A fluorometric skin-interfaced microfluidic device and smartphone imaging module for *in situ* quantitative analysis of sweat chemistry. *Lab Chip* **18,** 2178-2186 (2018).
50. S. Jayaraman, Flow cytometric determination of mitochondrial membrane potential changes during apoptosis of T lymphocytic and pancreatic beta cell lines: Comparison of etramethylrhodamineethylester (TMRE), chloromethyl-X-rosamine ($H_2$-CMX-Ros) and MitoTracker Red 580 (MTR 580). *J. Immunol. Methods* **306,** 68-79 (2005).
51. Y. Qian, J. Lin, L. Han, L. Lin, H. Zhu, A resorufin-based colorimetric and fluorescent probe for live-cell monitoring of hydrazine. *Biosens. Bioelectron.* **58,** 282-286 (2014).
52. C. A. Schneider, W. S. Rasband, K. W. Eliceiri, NIH image to ImageJ: 25 years of image analysis. *Nat. Methods* **9,** 671-675 (2012).
53. D. F. Swinehart, The Beer-Lambert law. *J. Chem. Educ.* **39,** 333-335 (1962).
54. S. P. Lee *et al*., Highly flexible, wearable, and disposable cardiac biosensors for remote and ambulatory monitoring. *NPJ Digit. Med*. **1**, 2 (2018).
55. H. Joeng *et al*., Modular and Reconfigurable Wireless E-Tattoos for Personalized Sensing. *Adv. Mater. Technol*. **4**, 1900117 (2019).
56. R. Vetrugno, R. Liguori, P. Cortelli, P. Montagna, Sympathetic skin response. *Clin. Auton. Res.* 13, 256-270 (2003).
57. N. Gerrett, B. Redortier, T. Voelcker, G. Havenith, A comparison of galvanic skin conductance and skin wittedness as indicators of thermal discomfort during moderate and high metabolic rates. *J. Therm. Biol.* 38, 530-538 (2013).
58. J. E. Wingo, D. A. Low, D. M. Keller, R. M. Brothers, M. Shibasaki, C. G. Crandall, Skin blood flow and local temperature independently modify sweat rate during passive heat stress in humans. *J. Appl. Physiol*. **109**, 1301-1306 (2010).
59. T. Amano, N. Gerrett, Y. Inoue, T. Nishiyasu, G. Havenith, N. Kondo, Determination of the maximum rate of eccrine sweat glands' ion reabsorption using the galvanic skin conductance to local sweat rate relationship. *Eur. J. Appl. Physiol.* **116**, 281-290 (2016).
60. A. K. M. Shamsuddin, T. Kuwahara, A. Oue, C. Nomura, S. Koga, Y. Inoue, N. Kondo, Effect of skin temperature on the ion reabsorption capacity of sweat glands during exercise in humans. *Eur. J. Appl. Physiol.* **94,** 442-447 (2005).
61. M. J. Buono, K. D. Ball, F. W. Kolkhorst, Sodium ion concentration vs. sweat rate relationship in humans. *J. Appl. Physiol.* **103,** 990-994 (2007).

62. M. J. Buono, R. Claros, T. DeBoer J. Wong, $Na^+$ secretion rate increases proportionally more than $Na^+$ reabsorption rate with increases in sweat rate. *J. Appl. Physiol.* **105,** 1044-1048 (2008).
63. M. Fenske, Determination of cortisol in human plasma by thin-layer chromatography and fluorescence derivatization with isonicotinic acid hydrazide. *J. Chromatogr. Sci.* **46,** 1-3 (2008).
64. L. Plat *et al*., Metabolic effects of short-term elevations of plasma cortisol are more pronounced in the evening than in the morning. *J. Clin. Endocrinol. Metab.* **84,** 3082-3092 (1999).
65. B. M. Kudielka, S. Bellingrath, D. H Hellhammer, Further support for higher salivary cortisol levels in “morning” compared to “evening” persons. *J. Psychosom. Res.* **62,** 595-596 (2007).
66. J. C. Wingfield, Ecological processes and the ecology of stress: the impacts of abiotic environmental factors. *Funct. Ecol*. **27**, 37-44 (2013).
67. A. H. Marques, M. N. Silverman, E. M. Sternberg, Evaluation of stress systems by applying noninvasive methodologies: measurement of neuroimmune biomarkers in the sweat, heart rate variability and salivary cortisol. *Neuroimmunomodulation* **17,** 205-208 (2010).
68. Nordmann et al., Muscle-Derived IL-6 Is Not Regulated by IL-1 during Exercise. A Double Blind, PlaceboControlled, Randomized Crossover Study. PLoS One, 0139662 (2015).
69. M. -Y. Seo, S. -M. Lee, Protective effect of low dose of ascorbic acid on hepatobiliary function in hepatic ischemia/reperfusion in rats. *J. Hepatol.* **36,** 72-77 (2002).
70. K. Ohara, Chloride concentration in sweat; its individual, regional, seasonal and some other variations, and interrelations between them. *J. Physiol. Sci.* **16,** 274-290 (1966).
71. T. Fukumoto, T. Tanaka, H. Fujioka, S. Yoshihara, T. Ochi, S. Kuroiwa, Differences in composition of sweat induced by thermal exposure and by running exercise. *Clin. Cardiol.* **11,** 707-709 (1988).
72. M. A. Baker, Effects of dehydration and rehydration on thermoregulatory sweating in goats. *J. Physiol.* **417,** 421-435 (1989).
73. K. Sato, W. H. Kang, K. Saga, K.T. Sato, Biology of sweat gland and their disorders. I. Normal sweat gland function. *J. Am. Acad. Dermatol*. **20**, 537-563 (1989).
74. S. M. Fortney, C. B. Wenger, J. R. Bove, E. R. Nadel, Effect of hyperosmolality on control of blood flow and sweating. *J. Appl. Physiol.* **57,** 1688-1695 (1984).
75. S. Brody et al., A randomized controlled trial of high dose ascorbic acid for reduction of blood pressure, cortisol, and subjective responses to psychological stress. *Psychopharmacol.* **159**, 319-324 (2002).

## Figures and captions

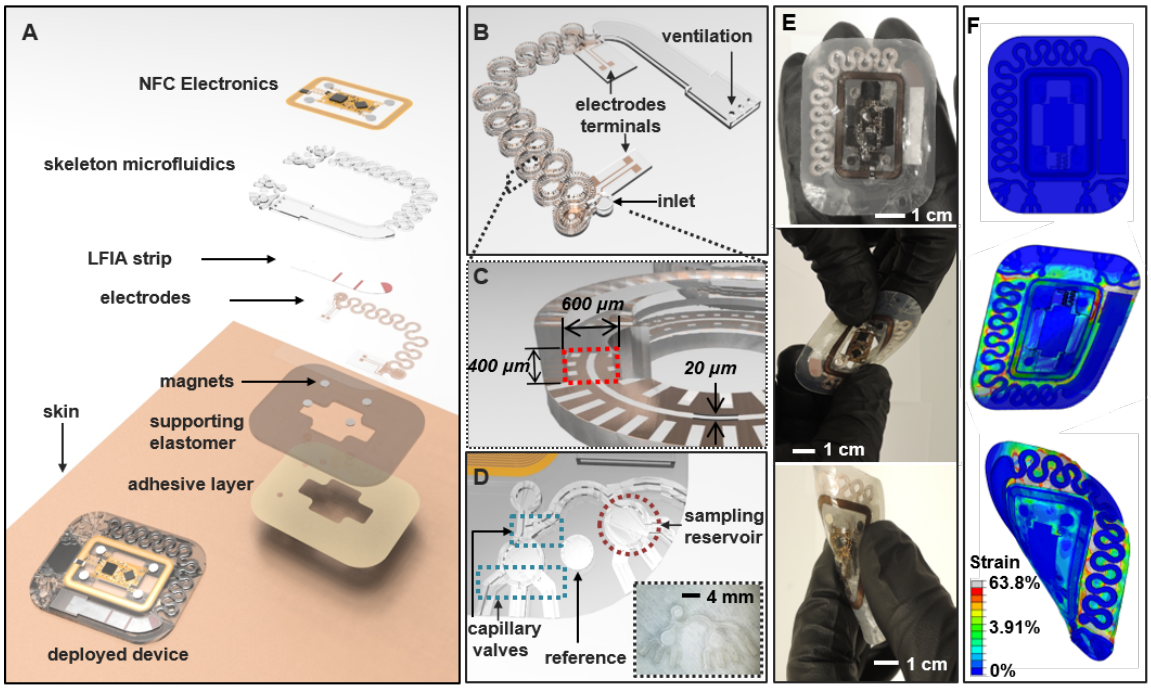


**Fig. 1** Schematic illustrations and optical images of a skeletal microfluidic device for immunoassays for cortisol, fluorescence assays for glucose and ascorbic acid (vitamin C) and electrical interfaces for sweat loss, sweat rate and galvanic skin response. (*A*) Exploded schematic illustration of the structure of the device. (*B*) Magnified view of the main serpentine skeletal channel for tracking sweat loss, sweat rate, and an immunoassay for cortisol. (*C*) Cross-sectional view of the main channel, highlighting channel dimensions and integrated electrodes. (*D*) Microfluidic structures for fluorescence assays of glucose and ascorbic acid and an optical image of the system (inset). (*E*) Optical image of an assembled device (top), and undergoing mechanical twisting (middle) and bending (bottom). (*F*) 3D modeling of the mechanics associated with similar configurations: flat (undeformed; top), twisted (middle) and bent (bottom) to show the corresponding distributions of strain.

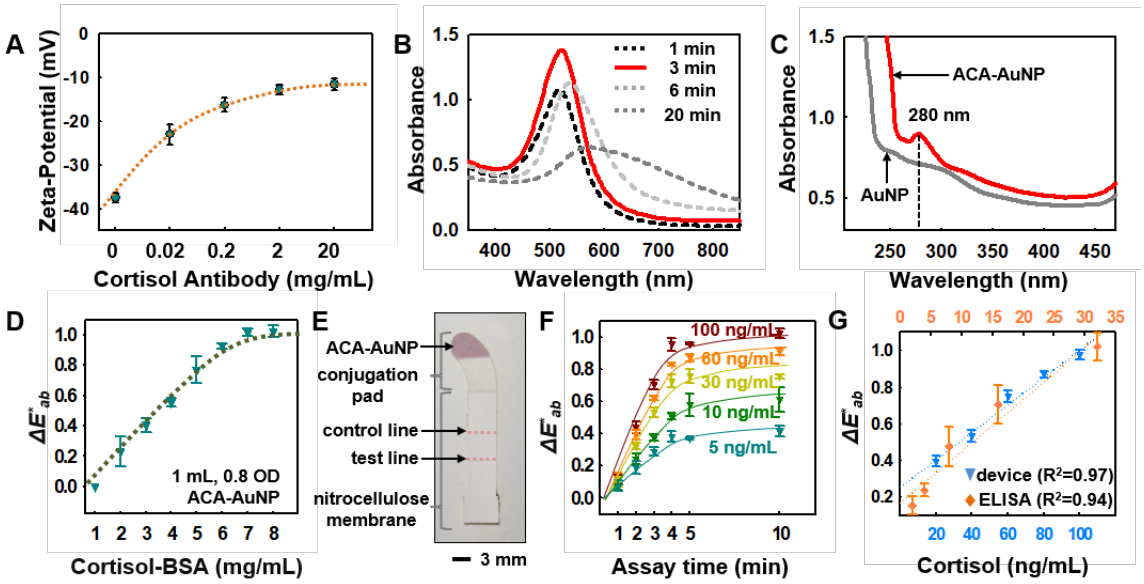


706

707 **Fig. 2** Immunoassay-based lateral flow design and measurements for sweat cortisol. (*A*) Zeta
708 potential values measured after conjugation of ACA (0, 0.02, 0.2, 2 and 20 mg/mL; 3 data points
709 for each ACA concentration; N=15) on 30-nm AuNPs. (*B*) Effects of ACA (0.5 mg/mL) conjugation
710 time on absorbance. (*C*) Comparison of absorbance at a wavelength of ~280 nm before and after
711 ACA conjugation. (*D*) Color development of ACA-AuNP at various concentrations of cortisol-BSA
712 on the NC membrane. (*E*) Optical image of the lateral flow immunoassay strip after assembly and
713 laser cutting. (*F*) Color development trends at various cortisol concentrations (5, 10, 30, 60 and
714 100 ng/mL) as a function of time. (*G*) Calibration of color index from the device at various
715 concentrations of cortisol (20, 40, 60, 80 and 100 ng/mL) and comparisons to bench-top ELISA
716 tests at concentrations of 2, 4, 8, 16 and 32 ng/mL.

717

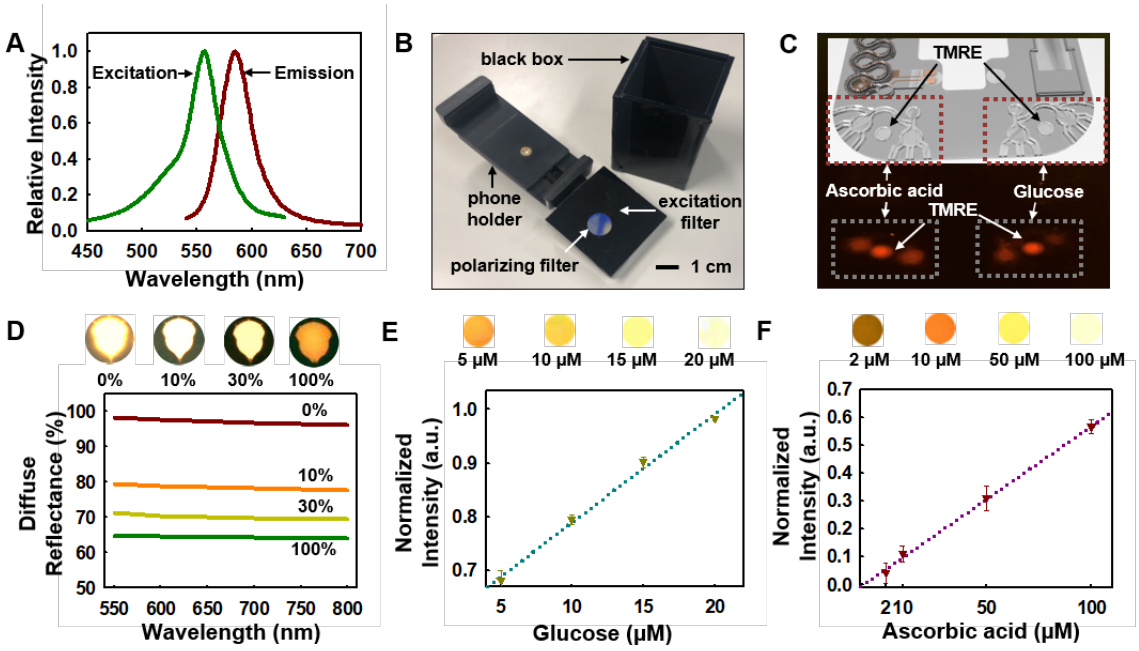


718

719 **Fig. 3** Fluorescence assay design and measurements for sweat glucose and ascorbic acid. (*A*)
720 Excitation and emission curves of OxiRed, the fluorescence probe. (*B*) Optical image of the
721 apparatus used for fluorescence readout. (*C*) Image of ascorbic and glucose signals along with
722 the reference (TMRE) signal. (*D*) Effect of the silicone packaging on the fluorescent signal for
723 various ratios at black and white pigments at 0:10, 1:9, 3:7 and 10:0 (0, 10, 30 and 100%,
724 respectively), along with corresponding images (top). (*E*) Plot of the normalized fluorescence
725 intensity for various glucose concentrations at 0.1, 0.5, 1, 2 µM and their fluorescence intensities
726 from associated images (top). (*F*) Plotting of normalized fluorescence intensity for various ascorbic
727 acid concentrations at 5, 10, 50, 100 µM concentrations and their fluorescence intensities from
728 associated images (top).

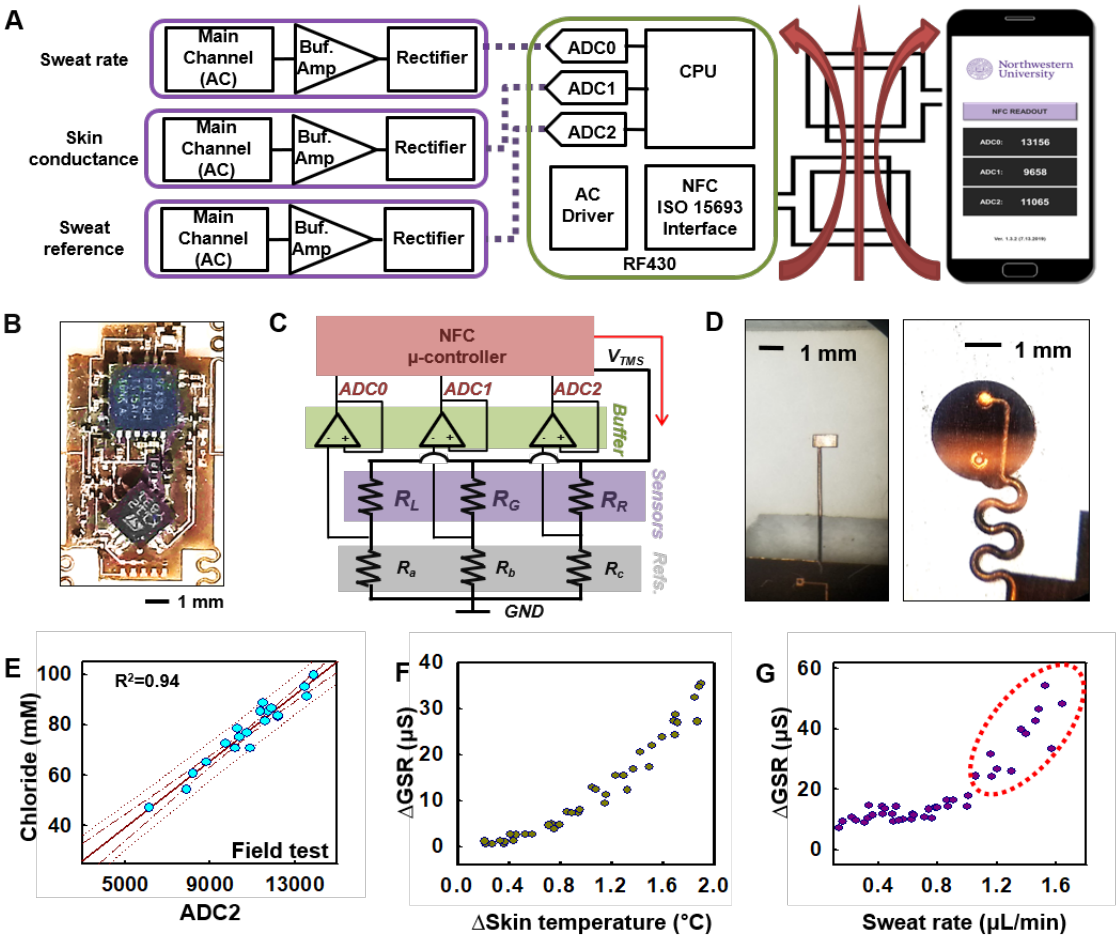


729

730 **Fig. 4** Design of NFC electronics for monitoring sweat loss, sweat rate, and GSR. (*A*) Schematic
731 block diagram of the NFC electronic system and its interface to a sweat microfluidic device and a
732 smartphone. (*B*) Optical image of the electronics to show chip placement. (*C*) Schematic block
733 diagram of the electronics to show the reference resistor layouts for the main, reference, and GSR
734 readout. (*D*) Magnified optical images of the electrode terminals for GSR (left) and tracking-
735 reference to the microfluidic device (right). (*E*) Plot of electrolyte concentration for a series of
736 samples of human sweat in the reference microchannel and corresponding ADC2 values
737 determined by wireless readout. (*F*) Effect of body temperature at the initial phase of exercise on
738 ΔGSR. (*G*) Correlation between sweat rate and ΔGSR after skin temperature stabilizes and
739 sweating begins (forearm, 18-20°C temperature, and 15-30% humidity).

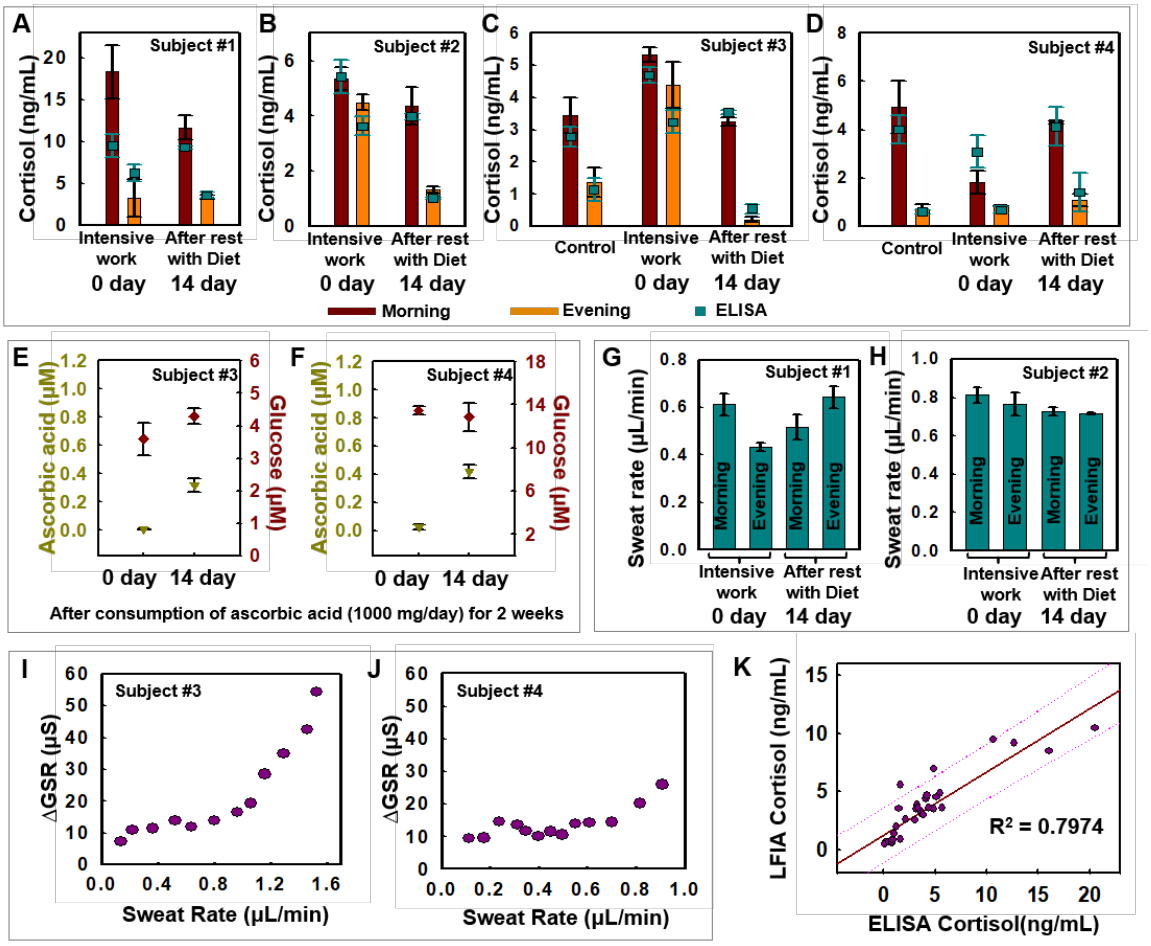


**Fig. 5** On-body measurements of sweat biomarkers during exercise. (*A*-*D*) Cortisol lateral flow immunoassay results for subjects #1 and #4 at 0 and 14 days. 'Control' (*C*, *D*) indicates measurements of sweat cortisol under normal conditions of that the subjects are not stressed. (*E*, *F*) Results of ascorbic acid and glucose at 0 and 14 days for subjects #3 and #4. (*G*, *H*) Sweat rate measurements for subjects #1 and #2 at 0 and 14 days. (*I*, *J*) ΔGSR measurements during high intensity exercise and sweating for subjects #3 and #4. (*K*) Plotting and regression of quantitative assays results from LFIA and ELISA. Dotted line is prediction line.